

Article

Elucidating the Effects of Hydrothermal Alteration on Seismic Reflectivity in the Footwall of the Lalor Volcanogenic Massive Sulfide Deposit, Snow Lake, Manitoba, Canada

Ernst Schetselaar *, Gilles Bellefleur  and Patricia Hunt

Geological Survey of Canada, 601 Booth Street, Ottawa, ON K1A 0E8, Canada; gilles.bellefleur@canada.ca (G.B.); pat.hunt@canada.ca (P.H.)

* Correspondence: ernst.schetselaar@canada.ca; Tel.: +1-613-762-8725

Received: 2 May 2019; Accepted: 19 June 2019; Published: 25 June 2019



Abstract: The integrated analysis of seismic rock properties, lithochemical data, and mineral compositional data, estimated via scanning electron microscopy-energy dispersive X-ray spectroscopy (SEM-EDS), provides insight into the effects of hydrothermal alteration on seismic reflectivity in the footwall of the Lalor volcanogenic massive sulfide (VMS) deposit, Manitoba, Canada. The effects of hydrothermal alteration on variations in acoustic impedance are secondary in magnitude and superimposed on the dominant acoustic impedance contrast between felsic and mafic volcanic protoliths. This secondary effect is due to an increase in P-wave velocity with increasing intensity of hydrothermal alteration, as measured by the Ishikawa and Carbonate-Chlorite-Pyrite alteration indices. Mixture modeling of the seismic rock properties and mineral percentages suggests that the increase in seismic velocity is due to an increase in abundance of cordierite, which is one of the diagnostic aluminum silicates for hydrothermally-altered volcanic rocks metamorphosed in the upper almandine amphibolite facies. The synthetic seismic data of a simple VMS model consisting of mafic-felsic host rock contacts, a sulfide ore lens, and a discordant hydrothermal conduit, consisting of the amphibolite-facies mineral assemblage (600 °C, 6 kbar) encountered at Lalor, show enhanced seismic reflections at conduit-host rock contacts, in comparison to its greenschist facies equivalent (350 °C, 2.5 kbar). This zone of enhanced seismic reflectivity in the footwall of the massive sulfide ore zone is also recognized on the Lalor seismic data suggesting that high-grade terrains hosting VMS deposits possess enhanced potential for the seismic detection of their footwall hydrothermal alteration zones.

Keywords: seismic rock properties; hydrothermal alteration minerals; volcanogenic massive sulfide deposits; mixture modeling

1. Introduction

For the past three decades, the seismic reflection method has shown promising results for the exploration of volcanogenic massive sulfide (VMS) deposits [1–3]. This success is largely attributable to their ore composition of high-density sulfide minerals, including low-seismic velocity minerals, such as chalcopyrite, pyrrhotite, sphalerite, and high-velocity pyrite. The sulfide-dominant compositions of these deposits generally result in high impedance contrasts at contacts with their silicate-dominant volcanogenic host rocks [1,2]. Although the direct detection of sulfide ore will likely remain the primary objective of any 3D seismic exploration endeavor, seismic imaging of the more regional-scale hydrothermal alteration system associated with VMS deposits may provide important geological insight, widening the scope of seismic exploration from direct detection to indirect targeting in areas

with favorable but yet undemonstrated potential. Indirect targeting is a viable option in cases where sulfide ore lenses have limited thickness and lateral extent due to primary ore forming conditions or subsequent tectonic dismemberment, rendering their seismic detection challenging. Alternatively, dependent on the design of the survey, tectonic processes may have steepened the ore zone, which may also hamper their seismic detection.

This paper reports the integrated modeling of seismic rock properties, lithogeochemistry, and estimates of mineral abundance from scanning electron microscopy-X-ray energy dispersive spectroscopy (SEM-EDS) to gain more insight into the largely unknown potential of detecting VMS-related hydrothermal alteration. The objective here is to widen the perspective from the seismic properties of the sulfide ore minerals to the silicate-dominant mineral assemblages of VMS-proximal hydrothermal conduits.

First, we analyze the relationships between seismic rock property logs, lithofacies logs, and drill core lithogeochemistry, providing insight into the effect of protolith composition and the intensity of hydrothermal alteration on seismic rock property variations. Secondly, we model the seismic properties of mineral mixtures by estimating their abundances from SEM-EDS images of thin sections cut from 11 drill core samples. When these estimates are combined with the appropriate mineral velocities and densities, the mixture-modeled P-wave velocity and density can be computed, which can then be compared with the seismic rock property measurements of these samples. Collectively, the estimated mineral percentages and modeled seismic rock properties allow the elucidation of which minerals play a dominant role in producing the observed effects of hydrothermal alteration on the P-wave velocity and density measurements. Thirdly, we compare the seismic response of synthetic models of VMS ore systems metamorphosed in the lower greenschist and amphibolite facies to assess the effects of metamorphic grade on the potential for detecting hydrothermal alteration zones in seismic data. Finally, on the basis of these results, we revisit previously reported interpretations of the 3D seismic cube acquired over the Lalor VMS deposit [4,5] to investigate if the response of hydrothermal alteration can actually be recognized in the seismic data.

2. Geological Setting

The Lalor volcanogenic massive sulfide (VMS) deposit is located near Snow Lake, Manitoba, Canada, about 700 km north of Winnipeg, and is hosted in the volcanic, volcanoclastic, and intrusive rocks of the Snow Lake arc assemblage of the Paleoproterozoic Flin Flon greenstone belt (Figure 1).

The Snow Lake arc assemblage comprises a 6 km thick section of three volcanic successions, displaying a geodynamic evolution from a primitive arc (Anderson sequence to the south) to a mature arc (Chisel sequence) to an arc-rift (Snow Creek sequence to the northeast) setting [6]. The 1.89 Ga volcanic sequences were intruded by 1.88–1.84 Ga successor-arc felsic and mafic plutons, deformed by isoclinal folds and thrusts, and subsequently interleaved with their 1.86–1.84 Ga successor arc sedimentary cover by continued fold-thrust style tectonics [7,8], during which the peak upper almandine-amphibolite facies metamorphic conditions were reached at approximately 1.82–1.81 Ga [6].

VMS deposits in the Snow Lake arc sequence mainly occur within the Anderson and Chisel sequences. In contrast to the Cu-rich VMS-deposit hosted in the Anderson sequence, most VMS deposits in the Chisel sequence are Zn-rich and are dominantly hosted in mafic and intermediate to felsic volcanic and volcanoclastic rocks. The Chisel sequence has been subdivided into the lower and upper subsequences [9], forming the footwall and hanging wall, respectively, of a structural contact 10–200 m above the massive sulfide ore lenses of the Zn-rich VMS deposits (Chisel, Chisel North, Ghost, Lost, and Lalor, Figure 1). This contact has been tentatively interpreted as a thrust fault on the basis of the contrasting lithogeochemical trace element signatures of its hanging wall and footwall sequences, and an abrupt change in dip, which is associated with opposing facing directions [6].

A large subconcordant hydrothermal alteration system, developed in the footwall of the Zn-rich VMS deposit, is closely associated in space and time to the magmatic evolution of the Richards subvolcanic intrusion [10,11] (Figure 1). Disconformable alteration zones that can be traced to the

Chisel, Chisel North, and Lalor deposits are rooted within it [10,11]. The footwall hydrothermal alteration in the Lower Chisel subsequence evolved in two stages. The first stage produced a semi-conformable zone of albitization, silicification, and epidotization, 1–2 km below the deposits that are spatially associated with synvolcanic dykes and intrusions. The second stage produced sub-concordant zones of intense hydrothermal alteration in the immediate footwall of the massive sulfide deposits marking their feeder conduits [10,11]. These hydrothermally-altered rocks were, after metamorphism in the amphibolite facies, transformed into schist and gneiss with aluminum-silicate porphyroblasts of garnet, staurolite, cordierite, kyanite and anthophyllite [10–12]. Alteration in close proximity to the sulfide ore zones at Lalor also includes pervasive zones of finely disseminated sulfides (pyrite, pyrrhotite, sphalerite, chalcopyrite, and galena) associated with carbonate, tremolite, talc, and chlorite-rich rocks [10,12]. Four chemical associations can be distinguished in the zone of intense hydrothermal alteration in the footwall of the Lalor VMS deposit on the basis of metamorphic mineral assemblages (Table 1). These mineral assemblages reflect lithogeochemical variations of different volcanic protoliths, as well as metasomatism during hydrothermal alteration and subsequent metamorphic crystallization [12].

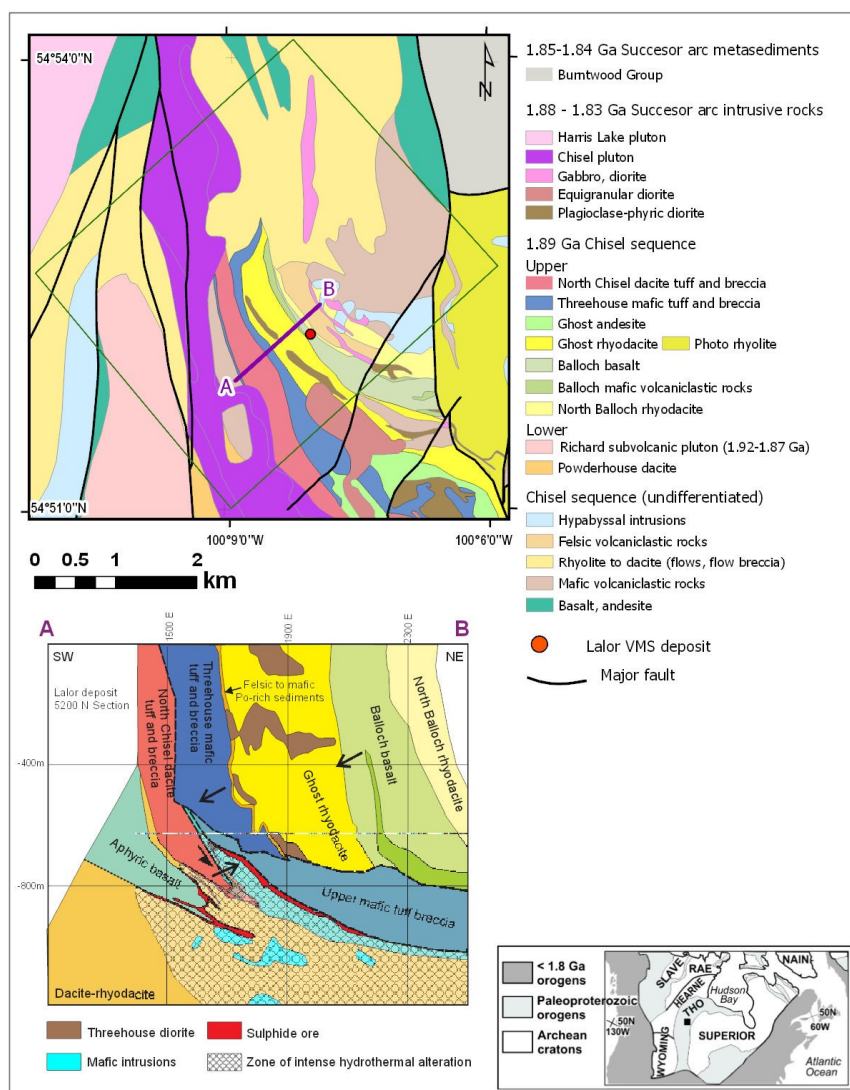


Figure 1. Geological map of the Chisel basin with a SW–NE-oriented cross section of the Lalor volcanicogenic massive sulfide (VMS) deposit generalized after [9]. The rectangle on the map shows the outline of the 3D seismic survey. The inset shows the tectonic map of the Canadian Shield, including the Trans-Hudson orogen (THO). The black square indicates the location of the study area.

Table 1. Chemical associations differentiated in the footwall hydrothermal alteration zone of the Lalor VMS deposit after [12].

Chemical Association	Minerals
K	sericite, pyrite, biotite, kyanite
K–Fe, Mg	quartz, biotite, kyanite
Fe, Mg	anthophyllite, cordierite, garnet, biotite, staurolite
Ca, Mg	carbonate, chlorite ± Ca–Mg amphiboles
Less intense alteration	Variable

The Lalor deposit consists of 12 mineralized zones, starting at a vertical depth of 570 m and extending down to approximately 1160 m. The mineralization zones trend to the northwest and have dips between 10° and 30° to the NNE. They are generally thin (average thickness is less than 12 m) and vary in size and grade. The deposit comprises six zinc-rich and six gold-rich zones [13]. The zinc-rich zones are the largest and shallowest zones of the deposit, and generally comprise near-massive to massive sulfide mineralization. Sulfides in the zinc-rich zones dominantly consist of pyrite crystals and sphalerite that is interstitial to the pyrite. The deposit also includes six gold-rich zones below the Zn-rich zones in the footwall rocks. The gold zones (including 8.8 Mt at 4.6 g/t Au: [13,14]) are disseminated with some stringers of sulfide mineralization. These zones contain a low amount of iron sulfide, typically less than 4–5%. The deepest gold zones are also associated with higher copper grades (average grade of 4.64% Cu), suggesting that these may represent feeder zones of the VMS ore system.

The ore lenses of the Lalor deposit, together with the host rocks, were affected by a polyphase deformation history of isoclinal folding and thrust faulting. The main foliation is a S2 penetrative mineral shape to gneissic fabric, with local evidence of the transposition of F1 isoclinal folds [8,15]. The F2 folds are also isoclinal, verging towards the south and involving the upper massive sulfide ore lenses. The F2 folds were refolded by open N–NE upright F3 folds, locally resulting in Type 1 [16] fold interference patterns [15]. The limbs of these fold structures are locally attenuated by shear zones, often displaying the boudinage of competent rock units and quartz-carbonate veins (see [17] for the nomenclature used for labelling fold structures and associated foliations in rocks affected by multiple phases of deformation).

3. Integrated Analyses of Seismic Wireline Logs and Drill Core Lithochemistry

The wireline log data acquired in ten boreholes located close to or intersecting the deposit were used in previous interpretations to show that massive sulfide mineralization and felsic-mafic host rock contacts generate the dominant high-amplitude seismic reflections at Lalor [4,5] (see also Section 6). Herein, we reanalyze the wireline logs to investigate the additional effects of hydrothermal alteration on acoustic impedance contrast. Since the majority of seismic surveys in hard rock exploration, including the Lalor seismic cube, focus on P-wave reflectivity, shear wave velocities were excluded from the analysis.

The results obtained from the wireline logs were in general supported with P-wave velocity and density measurements on core samples, although some differences were observed between the two types of measurements. The γ - γ density logs showed a strong correlation ($r = 0.85$, $n = 23$) with co-located density measurements of drill core samples [18]. The sonic wireline logs, however, were not collocated with the core samples that were subjected to seismic velocity measurements. Nevertheless, a comparison of drill core P-wave velocity measurements with interpolated P-wave velocity values of a 3D grid model obtained by kriging the wireline log data yielded a root mean square error of 0.29 km/s ($n = 27$) [5]. All drill core samples subjected to the SEM-EDS analysis were previously subjected to seismic rock property measurements (Table 2), which allowed the modeling of seismic rock properties from the mineral volume fractions (see Section 4). For the procedures used in measuring these density and P-wave velocity measurements, refer to [5].

To investigate the additional effects of hydrothermal alteration on the acoustic impedance contrast, the samples of the ten wireline logs were co-registered with whole rock geochemical analyses from

drill core samples and their corresponding lithofacies using a threshold distance of 30 cm (Figure 2). These geochemistry and wireline log records were stored in a Microsoft Access® database compiled from the industry drill hole data. The co-registration was accomplished by matching records of the geochemistry drill core samples with records of the wireline logs on the distance along their corresponding drill paths (see Appendix A for the query syntax of this matching operation).

In any assessment of the effects of hydrothermal alteration on seismic reflectivity, it is important to separate the effects of hydrothermal alteration (and subsequent metamorphism) on the acoustic impedance contrast from those caused by variations in protolith composition. Therefore, our subdivision into lithofacies (e.g., a rock body having a unique definable compositional, textural, or structural character of genetic significance [19]) was based on the immobile element ratio of Zr/Ti, which allowed grouping the drill core samples into lithofacies with felsic, intermediate, and intermediate-mafic protolith compositions [20]. Each of these three lithofacies was further subdivided into least-altered and altered groups, using the above-described diagnostic metamorphic mineral assemblages of aluminum silicates, yielding a total of six classes. The advantage of this lithofacies classification is that it can be universally applied, regardless of the intensity of hydrothermal alteration and metamorphic overprint. This is particularly relevant for the gneisses and schists of the footwall hydrothermal alteration zone, where hydrothermal alteration and metamorphic crystallization destroyed the diagnostic observables of their volcanic protoliths.

The P-wave velocity (V_p) versus density (ρ) plot of the altered and least-altered lithofacies is shown in Figure 3. The overlay of the ellipses shown in Figure 3b were determined from the principal component analysis of the P-wave velocity and density wireline log data of each of the lithofacies. The ellipses represent the mean and scaled eigenvectors of the covariance matrix, such that the major and minor axes of the ellipses represent one standard deviation (i.e., 68%) of the V_p - ρ distributions. The locations and dimensions of the ellipses of mafic and felsic lithofacies in V_p - ρ space show that protolith composition dominantly controls the acoustic impedance contrast for both the least-altered and altered lithofacies. This is consistent with high-amplitude reflections observed at the contacts between least-altered felsic and mafic lithofacies [5] (Section 6). The second-order effects of hydrothermal alteration can be inferred by comparing the dimensions of the ellipses between the least-altered and altered lithofacies. Note that all the ellipses of the altered lithofacies are significantly larger in comparison to their least-altered equivalents. In addition, the altered lithofacies with intermediate to mafic protolith composition are oriented on a steeply sloping but slightly negative trend.

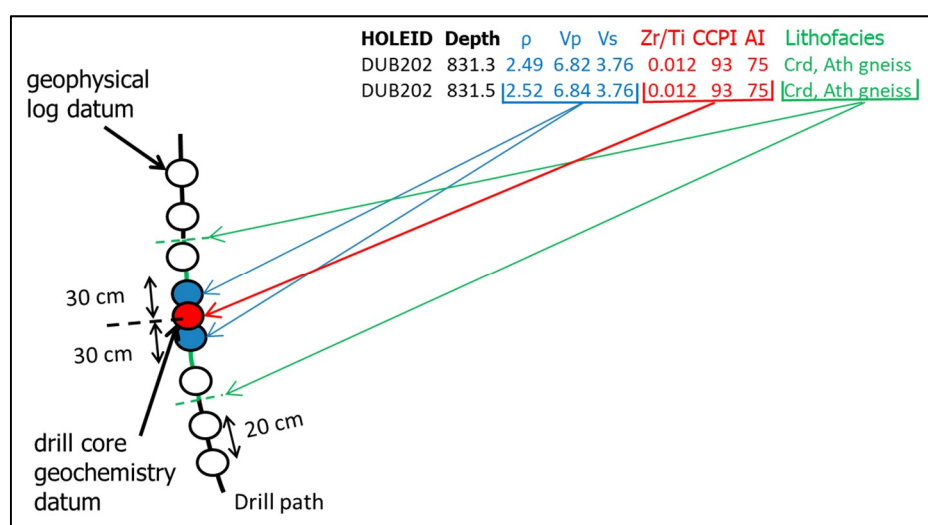


Figure 2. Schematic diagram showing the co-registration of the drill hole wireline log, lithochemical, and lithofacies log data.

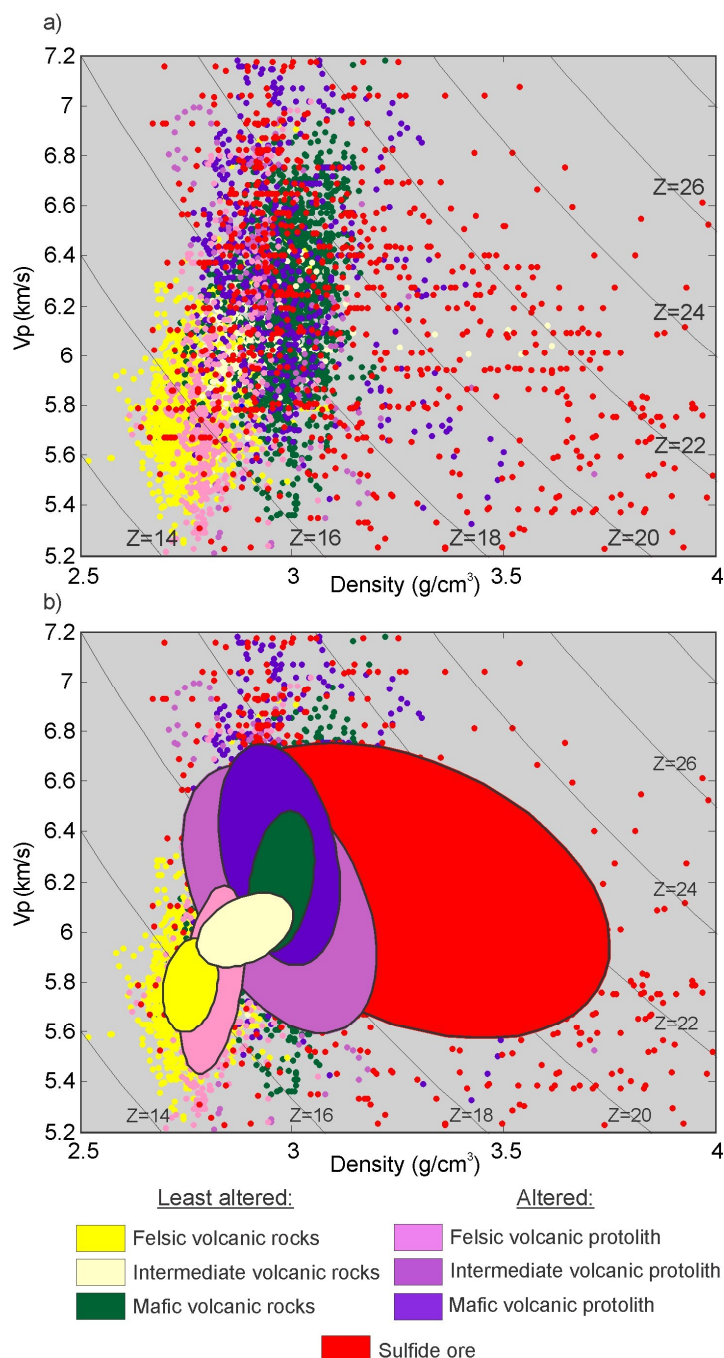


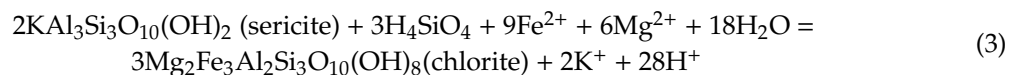
Figure 3. P-wave velocity (V_p) and density wireline log data of the main lithofacies units intersected in ten drill holes. (a) V_p - ρ plot of wireline log measurements; (b) as (a), with the overlay of ellipses defined by the principal component analysis of V_p and ρ for each lithofacies unit, with the minor and major axes representing one standard deviation from the mean. The mafic-intermediate lithofacies were defined by $Zr/Ti < 0.017$, the intermediate lithofacies by $0.017 \leq Zr/Ti < 0.030$, and the felsic lithofacies by $Zr/Ti \geq 0.03$. Ore, including disseminated, vein-type, near solid, and massive types of sulfide mineralization was based on drill log descriptions from Hudbay Minerals [4]. Lines of constant acoustic impedances (Z) in $kg/m^{-2}s^{-1} \times 10^{-6}$ are also shown on this figure.

In addition to the V_p - ρ lithofacies plot, the relationships between seismic rock property logs and alteration indices, computed from the co-registered whole rock geochemical analyses, were analyzed. These alteration indices included the Ishikawa index (AI) and chlorite-carbonate-pyrite (CCPI) index.

Both are commonly used as proxies for the intensity of hydrothermal alteration in VMS ore systems [21]. The Ishikawa index is defined as:

$$AI = \frac{([K_2O] + [MgO]) \times 100\%}{([K_2O] + [MgO] + [Na_2O] + [CaO])} \quad (1)$$

This index measures the breakdown of plagioclase feldspar and volcanic glass and their replacement by sericite (Equation (2)), and the subsequent replacement of sericite by chlorite (Equation (3)) [21]:



Because the AI index cannot differentiate between sericite and chlorite, a second alteration index, known as the chlorite-carbonate-pyrite index (CCPI) is usually computed:

$$CCPI = \frac{([MgO] + [FeO]) \times 100\%}{([MgO] + [FeO] + [Na_2O] + [K_2O])} \quad (4)$$

The CCPI increases with the formation of chlorite, Mg-Fe carbonate and pyrite. In combination, these indices measure the depletion of Na, Ca, gains of Fe, Mg, K and, indirectly, the relative enrichment of Al [21]. Because the Lalor VMS deposit was metamorphosed in the amphibolite facies, aluminum silicates of the K-Mg and Fe-Mg assemblages, such as cordierite, garnet, staurolite and biotite (Table 1) replaced the chlorite-rich greenschist facies alteration assemblages [20]. This prograde metamorphic replacement of chlorite has also been documented in footwall alteration zones of other VMS deposits in the Snow Lake region [22,23].

Figure 4 shows V_p - ρ plots of the AI and CCPI alteration indices computed from the drill core geochemical analyses of intermediate to mafic protoliths. Note the trends of higher AI and CCPI values with increasing velocity in these plots, which are consistent with the orientation of ellipses for altered lithofacies of intermediate to mafic composition (Figure 3). Both plots support the interpretation that the increasing velocity, decreasing density trend is associated with an increasing intensity of hydrothermal alteration.

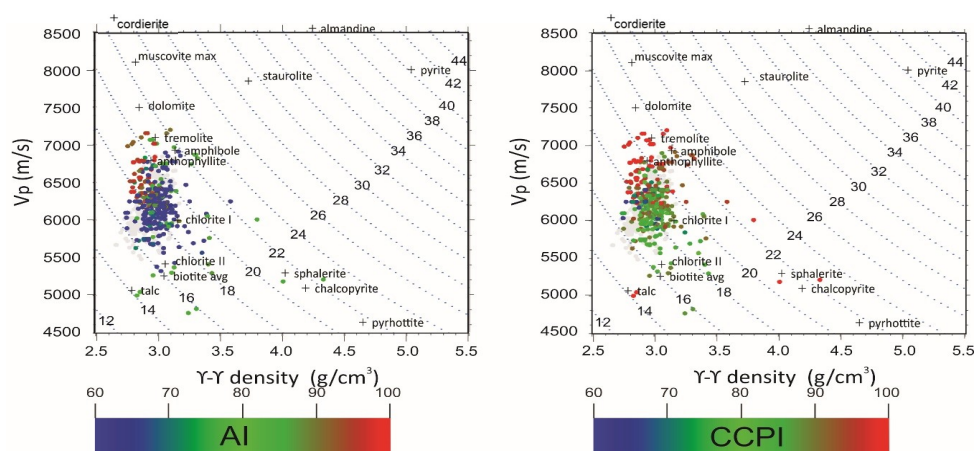


Figure 4. P-wave velocity (V_p) and density of rocks with mafic-intermediate volcanic protoliths from the footwall of the Lalor VMS deposit. Points are colored according to the Ishikawa (AI) and chlorite-carbonate-pyrite-index (CCPI) alteration indices. The isolines indicate acoustic impedance (Z) in $kg/m^{-2}s^{-1} \times 10^{-6}$.

4. Mixture Modeling of Seismic Rock Properties Using SEM-EDS Analyses

Searching for the minerals responsible for the negative low density-high P-wave velocity trend, eleven polished thin sections of 4.5×2.5 cm were cut from drill core samples of the footwall of the Lalor VMS deposit for scanning electron microscopy-energy dispersive X-ray spectroscopy (SEM-EDS). In the last two decades, SEM-EDS has gained popularity for identifying minerals and the quantification of their abundances [24]. The technique is based on mapping mineral grains by focusing an electron beam on a polished thin section and identifying the mineral species and chemical composition of each grain on the basis of peaks in the emitted X-ray energy spectra, each of them being unique to the atomic structure of the elements of which the mineral is composed. The reader is referred to [24] for an introductory review on the methodology and its applications, and to [25] for a discussion on the accuracy and caveats of SEM-EDS analysis.

The thin sections were cut normal to the foliation. Because no lineation was observed in the samples, it was assumed that the preferred mineral orientation, defining the foliation, interacted in an isotropic manner with these sections. This would justify equating the estimated mineral percentages from the thin sections with volumetric percentages, invoking the Delesse principle [26] and an unbiased randomized sampling design.

The thin sections were analyzed using the TESCAN MIRA3 Oxford SEM-EDS system [27]. This system includes the X-MAX 80 Silicon Drift Detector (Oxford Instruments, Oxford, UK), with AZtec Energy microanalysis software (Version 3.3, Oxford Instruments, High Wycombe, UK) [27]. The specialized module “Feature” of AZtec, which is particularly suited to large samples and routine analysis, was used to classify minerals from the EDS data. The individual mineral grains were identified using grey level thresholding of the backscattered electron images. The morphology and chemistry was then recorded for each grain, and each spectrum was immediately quantified and classified according to a user generated classification scheme. As many fields are recorded at high magnification as necessary to make up a large area and then montaged. The adjoining mineral grains were then reconstructed across the whole area [27]. With morphology and chemistry analyzed, the results enable a full calculation of the bulk mineralogy of the entire section, including the percentage of unclassified features (Figure 5, Table 3).

Given that the SEM-EDS analyses of the thin sections is limited to estimating mineral fractions, the modeling of seismic rock properties is bound by two limiting assumptions:

1. The seismic rock properties are completely defined by the seismic properties of the constituting mineral phases (i.e., the effects of porosity on seismic rock properties, including porosity due to microcracks, are negligible).
2. There is no preferential orientation of the mineral phases (i.e., the fabric of the rocks are homogeneous and quasi-isotropic).

Table 2. Seismic rock properties of drill core samples subjected to SEM-EDS analyses.

Sample	Lithology	Density	$V_p^{200 \text{ MPa}}$	$V_s^{200 \text{ MPa}}$
GSC-Lalor-MD-023	Ath-Crd-Grt gneiss	2.85	7.32	3.61
GSC-Lalor-MD-038	Rhyolite	2.72	6.33	3.77
GSC-Lalor-MD-039	Rhyolite	2.71	6.81	
GSC-Lalor-MD-041	Bt-St-Grt schist	2.94	6.86	3.63
GSC-Lalor-MD-099	Ath-Crd-Grt gneiss	3.00	6.94	3.83
GSC-Lalor-MD-110	Ath-Crd gneiss	2.86	7.57	4.01
GSC-Lalor-MD-156	Basalt	3.00	6.71	4.01
GSC-Lalor-MD-160	Qtz-Bt-Crd gneiss	2.77	6.77	4.03
GSC-Lalor-MD-165	Bt-Grt-Ath gneiss	2.88	6.24	3.69
GSC-Lalor-MD-188	Felsic tuff	2.86	6.18	3.77
GSC-Lalor-MD-218	Ath-Crd gneiss	2.86	7.20	4.08
	Mean	2.86	6.81	3.84

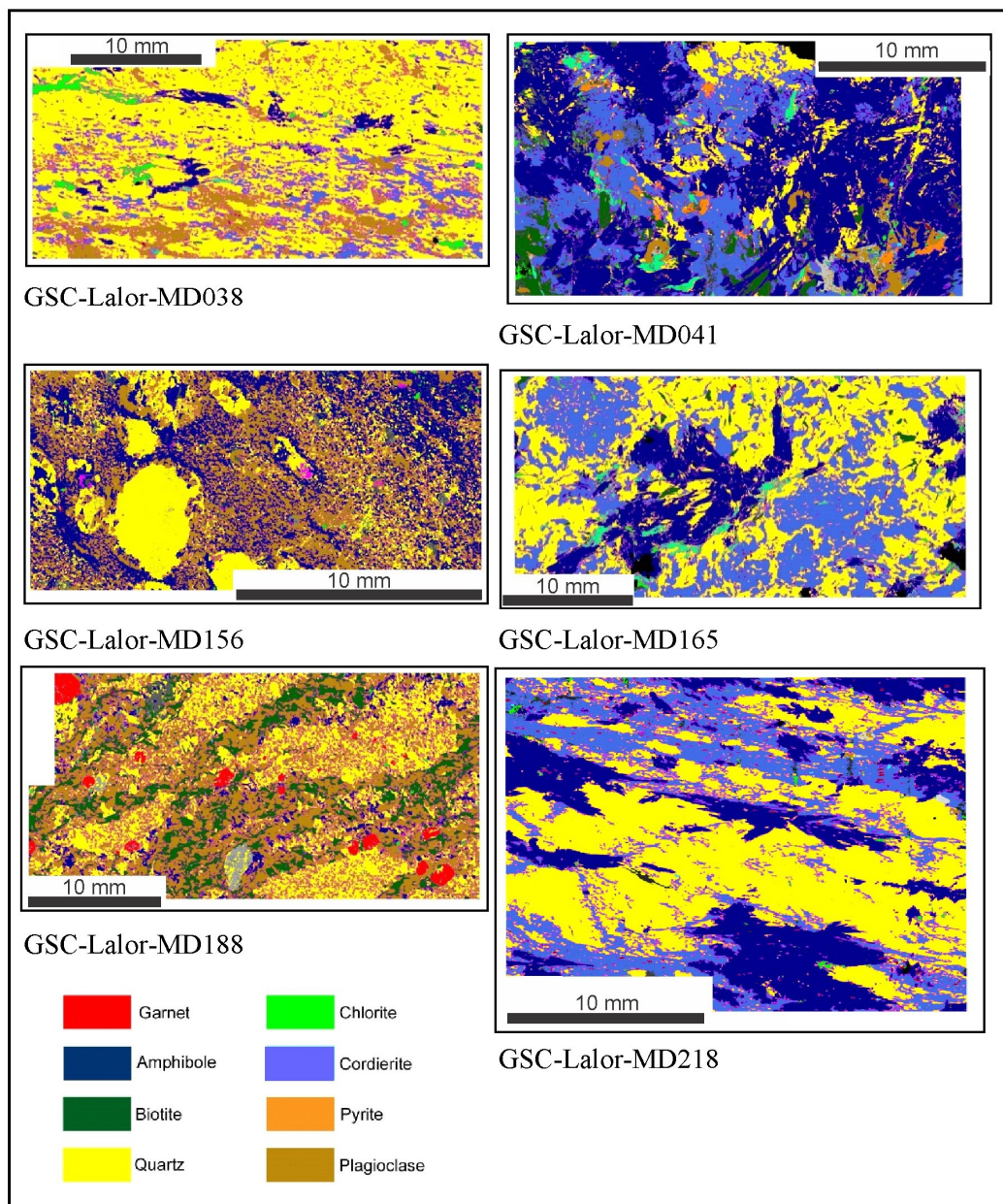


Figure 5. SEM-EDS mineral maps of six thin sections with sample identification.

Table 3. SEM-EDS analyses listing identified and classified minerals in percent.

Sample	Lithology	Am	An	Ap	Bt	Cal	Dol	Ccp	Chl	Crd	Ep	Gr	Grt	Hbl	Ilm	Py	Qtz	Rt	Sil	St	Udef	Total
GSC-Lalor-MD-023	Ath-Crd-Grt gneiss	8.9	7.2	0.2	10.7	0.1	0.0	0.1	1.1	36.3	0.0	0.1	7.6	0.0	0.4	1.0	24.3	0.0	0.0	0.0	2.3	100.3
GSC-Lalor-MD-038	Rhyolite	2.9	10.1	0.0	0.0	0.0	0.0	0.0	12.6	1.8	0.0	0.0	0.0	0.0	0.1	0.0	68.2	0.0	0.0	0.0	4.3	100.0
GSC-Lalor-MD-039	Rhyolite	0.0	1.6	0.0	7.7	0.0	0.0	0.0	0.1	0.0	0.0	0.1	0.0	0.0	0.0	0.6	81.6	0.0	1.3	2.2	5.0	100.1
GSC-Lalor-MD-041	Bt-St-Grt schist	53.2	0.0	0.2	4.8	0.0	0.0	0.0	2.0	21.7	0.0	0.0	0.0	0.0	0.4	3.1	11.7	0.0	0.0	1.0	1.9	100.0
GSC-Lalor-MD-099	Ath-Crd-Grt gneiss	17.9	8.9	0.5	2.0	0.0	0.0	0.0	1.8	19.9	0.0	0.0	13.7	0.1	0.8	2.4	29.9	0.0	0.0	0.2	1.9	100.0
GSC-Lalor-MD-110	Ath-Crd gneiss	46.7	0.0	0.3	6.3	0.0	0.0	0.0	11.2	27.4	0.0	0.0	0.0	0.1	0.8	1.4	3.7	0.5	0.0	0.5	1.1	100.1
GSC-Lalor-MD-156	Basalt	0.0	34.8	0.0	3.0	0.0	0.0	0.2	0.0	0.0	0.0	0.0	0.0	36.6	0.2	0.0	27.7	0.0	0.0	0.0	0.5	103.0
GSC-Lalor-MD-160	Qtz-Bt-Crd gneiss	7.5	0.0	0.4	29.6	0.0	0.0	0.0	1.8	20.4	0.0	0.0	0.0	0.0	1.7	0.0	37.4	0.0	0.0	0.0	1.0	100.0
GSC-Lalor-MD-165	Bt-Grt-Ath gneiss	14.9	0.0	0.2	1.3	0.0	0.0	0.0	2.7	32.7	0.0	0.0	0.0	0.0	0.6	0.0	45.8	0.0	0.0	0.0	1.8	100.0
GSC-Lalor-MD-188	Felsic tuff	5.5	38.7	0.1	18.8	0.0	0.0	0.0	0.0	0.0	0.0	0.0	2.6	0.0	0.1	0.0	32.9	0.0	0.0	0.0	1.4	100.0
GSC-Lalor-MD-218	Ath-Crd gneiss	24.1	0.0	0.2	0.0	0.0	0.0	0.0	0.0	26.2	0.0	0.0	0.0	0.0	0.6	0.1	48.3	0.0	0.0	0.0	0.6	100.0
	Mean	16.5	9.2	0.2	7.7	0.0	0.0	0.0	3.0	16.9	0.0	0.0	2.2	3.4	0.5	0.8	37.4	0.0	0.1	0.4	2.0	100.3

Under these assumptions, the effects of mineral composition on seismic rock properties can be modeled by combining the bulk mineral fractions f_i (Table 3) with their corresponding mineral P-wave velocities (V_{p_i}) and densities (ρ_i) (Table 4) to obtain mixture-modeled bulk seismic rock properties. The mixture-modeled density is defined as:

$$\rho_{\text{model}} = \sum_{i=1}^n f_i \rho_i \quad (5)$$

where f_i is the i th mineral fraction from the sum-normalized SEM-EDS analyses of n mineral components and ρ_i is the density of the i th mineral component.

Considering the lack of data for characterizing anisotropy, the best that can be done in modeling the P-wave velocity of the mineral mixture is to compute an average based on the theoretical lower and upper bounds of the mineral elastic moduli [28] (see [29] for a review of more advanced analysis, which includes statistics of mineral orientations to model the effects of anisotropy). Hence, the modeled P-wave velocity was computed from the mean bulk (\bar{K}) and shear ($\bar{\mu}$) moduli, known as the Hill averages of the Voigt and Reuss bounds [28]:

$$V_{P_{\text{model}}} = \sqrt{\frac{\bar{K} + \frac{4}{3}\bar{\mu}}{\rho_{\text{model}}}} \quad (6)$$

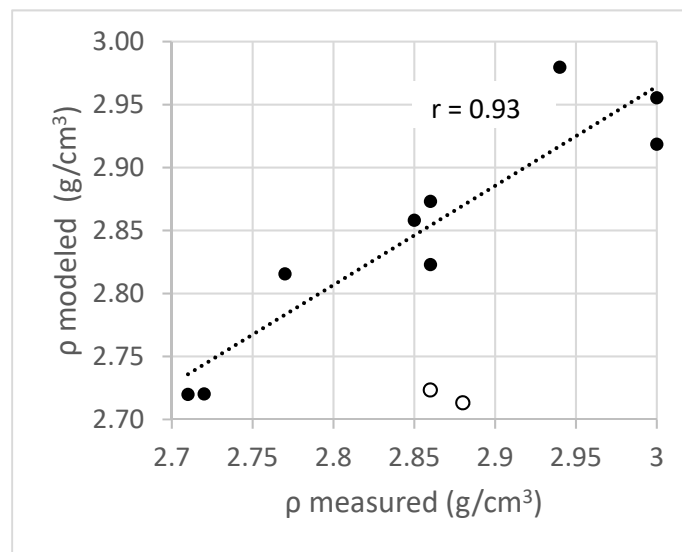
with:

$$\bar{K} = \frac{K_{\text{Voigt}} + K_{\text{Reuss}}}{2} = \frac{\sum_{i=1}^n (f_i K_{i_{\text{min}}}) + \sum_{i=1}^n \left(\frac{f_i}{K_{i_{\text{min}}}}\right)}{2} \quad (7)$$

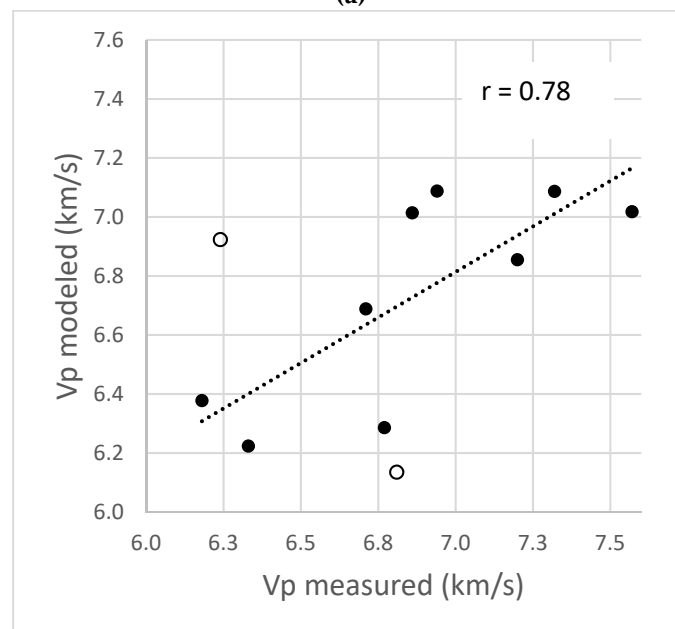
and:

$$\bar{\mu} = \frac{\mu_{\text{Voigt}} + \mu_{\text{Reuss}}}{2} = \frac{\sum_{i=1}^n (f_i \mu_{i_{\text{min}}}) + \sum_{i=1}^n \left(\frac{f_i}{\mu_{i_{\text{min}}}}\right)}{2} \quad (8)$$

A comparison between the measured and mixture-modeled seismic rock properties shows, with the exception of two outliers, a good fit for density (Figure 6a) and a reasonable fit for the P-wave velocity modeled as a linear mixture or the average of the Voigt and Reuss bounds (Table 5, Figure 6b,c). A V_p - ρ plot of the measured rock and mineral seismic properties, suggests, in combination with the estimated fractions that the most abundant minerals positioned beyond the extremes of the measured V_p - ρ distribution, along the approximately perpendicular biotite-cordierite and quartz-garnet bivariate mixture lines, dominantly control the seismic rock property variations (Figure 7). Although the SEM-EDS sample set is limited in size, the relatively large average abundance of low-density high-velocity cordierite (Figure 8a), and its positive correlation with P-wave velocity (Figure 8b), is consistent with the low-density trends of intensely-altered intermediate to mafic lithofacies (Figure 3), as well as increasing alteration index values towards higher velocities (Figure 4). Cordierite, among other aluminum silicates (such as garnet, kyanite, sillimanite, and staurolite), in volcanic protoliths is diagnostic for hydrothermally-altered rocks that have been metamorphosed in the middle to higher amphibolite facies [20,23]. Cordierite has a unique low density, high P-wave velocity signature in comparison to other silicate minerals, which explains the steep negative low density-high velocity trend (Figures 3, 4 and 7). In general, the SEM-EDS results confirm that the seismic rock property variations in the host rocks of the Lalor VMS deposit are controlled by large variations in the abundance of silicates, whereas the sulfides have negligible effects (Tables 2 and 3).



(a)



(b)

Figure 6. Scatter plots comparing the measured and modeled seismic rock properties. (a) Density; (b) P-wave velocity modeled by the average of the Voigt and Reuss bounds. Open circles indicate outliers not considered in the regression analysis.

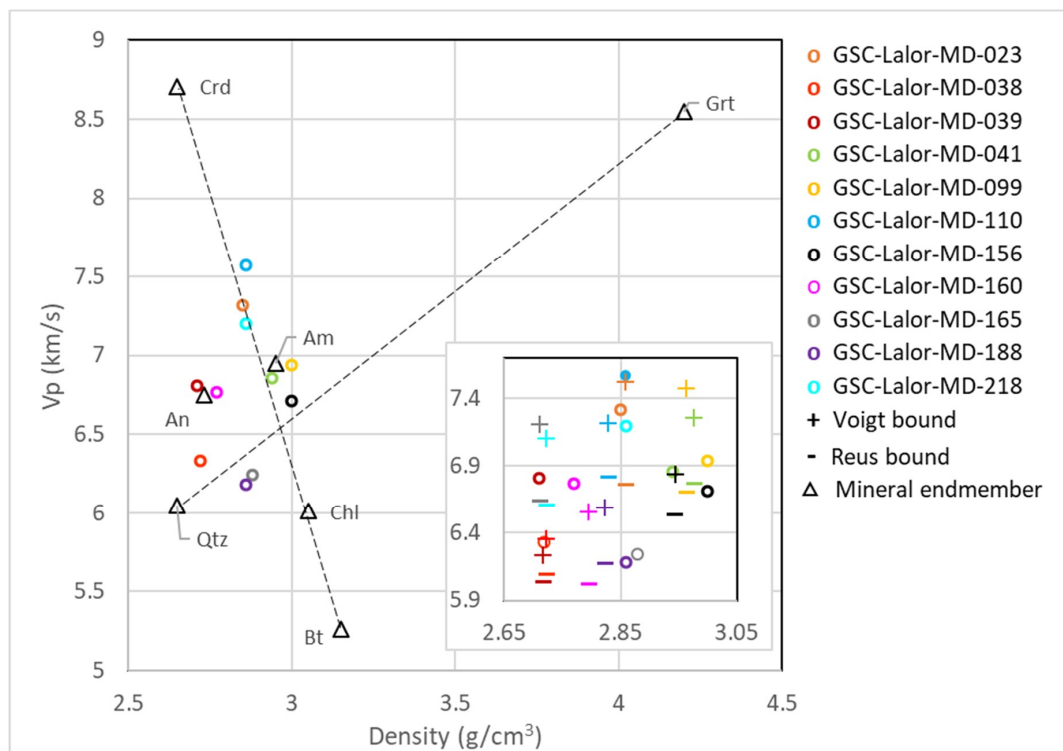
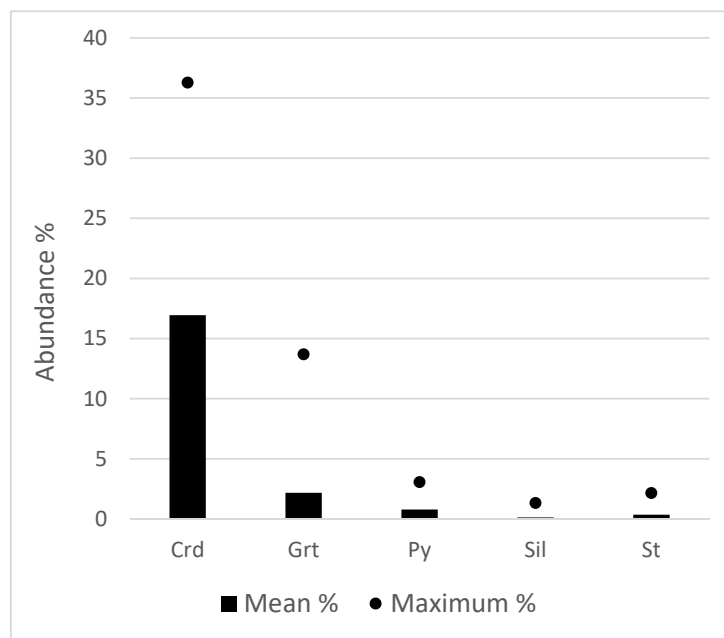


Figure 7. Plot of the seismic rock properties from the mixture modeling and endmembers (triangles) from the literature, corresponding to the minerals listed in Table 4. The inset shows mixture modeling estimates together with their modeled density-Voigt (+) and Reuss (−) P-wave velocity bounds.



(a)

Figure 8. Cont.

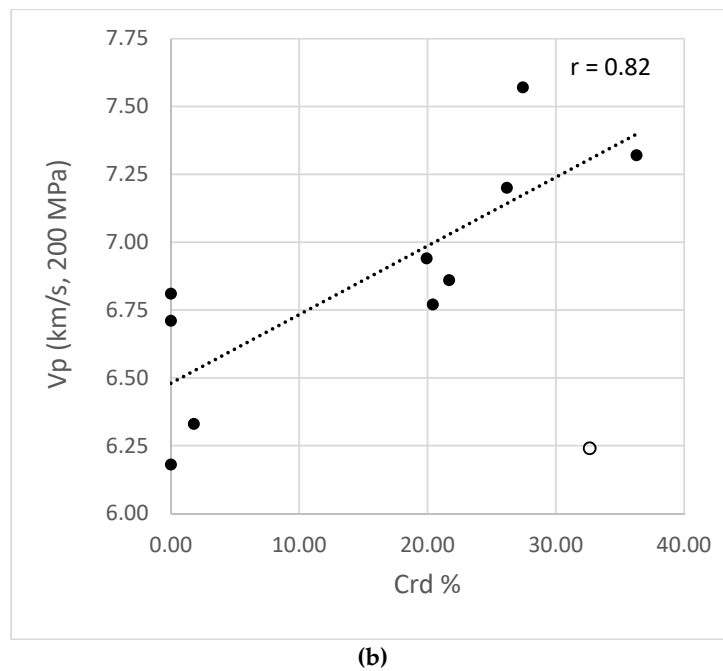


Figure 8. Summary of SEM-EDS analyses of high P-wave velocity minerals ($V_p > 7.5$ km) from samples of the hydrothermal alteration zone. (a) Volume fractions of high V_p minerals; (b) scatter plot showing the relationship between cordierite abundance and P-wave velocity.

Table 4. Seismic mineral properties.

Mineral	Abbr.	ρ (g/cm ³)	V_p (km/s)	V_p Anisotropy	V_s (km/s)	K (GPa)	m (GPa)
Albite	Ab	2.63 [28]	6.30 [30]	30.9% [30]	3.70 [30]	68.38	86.25
Anorthite	An	2.73 [31]	7.25 [30]	31.8% [30]	4.30 [30]	93.02	134.05
Amphibole	Am	2.95 [31]	6.95 [30]	23.8% [30]	3.85 [30]	98.77	103.02
Biotite	Bt	3.09 [31]	5.26 [30]		2.87 [30]	60.04	43.33
Chlorite	Chl	3.05 [31]	6.01 [32]		3.00 [32]	82.72	54.09
Cordierite	Crđ	2.65 [31]	8.71 [33]	14.2% [33]	4.51 [33]	147.14	177.16
Epidote	Ep	3.40 [28]	7.43 [28]	19.9% [30]	4.25 [30]	126.28	134.20
Garnet	Grt	4.20 [31]	8.55 [30]	0.9% [30]	4.75 [30]	212.27	192.91
Pyrite	Py	5.04 [34]	8.12 [34]		4.95 [34]	208.82	198.96
Quartz	Qtz	2.65 [32]	6.05 [32]	23.6% [30]	4.09 [32]	52.67	101.21
Sericite	Ser	2.81 [32]	6.30 [30]	44.2% [30]	3.75 [30]	72.01	88.59
Sillimanite	Sil	3.24 [31]	9.70 [30]	22.7% [30]	5.35 [30]	212.11	277.64
Staurolite	St	3.71 [31]	7.85 [30]	34.5% [30]	4.65 [30]	148.40	169.74

Table 5. Measured and modeled seismic rock properties.

Sample	$\rho_{meas.}$	ρ_{mod}	$V_{p200MPa}$	$V_{pmod-1m}$	V_{pVoigt}	V_{pReus}	V_{pVRavg}	K_{Voigt}	K_{Reus}	μ_{Voigt}	μ_{Reus}
GSC-Lalor-MD-023	2.85	2.86	7.32	7.35	7.48	6.67	7.12	93.02	69.26	50.33	45.95
GSC-Lalor-MD-038	2.72	2.72	6.33	6.25	6.27	6.06	6.16	49.73	44.41	42.91	41.61
GSC-Lalor-MD-039	2.71	2.72	6.81	6.10	6.15	5.97	6.06	43.49	40.17	44.47	42.61
GSC-Lalor-MD-041	2.94	2.98	6.86	7.20	7.27	6.83	7.06	91.66	78.62	49.52	45.38
GSC-Lalor-MD-099	3	2.96	6.94	7.27	7.44	6.70	7.07	92.11	66.78	53.68	49.48
GSC-Lalor-MD-110	2.86	2.87	7.57	7.20	7.23	6.94	7.08	91.91	83.65	43.55	41.15
GSC-Lalor-MD-156	3	2.92	6.71	6.80	6.84	6.60	6.72	72.15	62.88	48.18	48.05
GSC-Lalor-MD-160	2.77	2.82	6.77	6.44	6.51	6.02	6.26	65.60	52.78	40.21	36.88
GSC-Lalor-MD-165	2.88	2.71	6.24	7.07	7.16	6.60	6.88	76.74	57.25	46.71	45.70
GSC-Lalor-MD-188	2.86	2.82	6.18	6.49	6.55	6.21	6.38	61.87	54.10	44.42	41.01
GSC-Lalor-MD-218	2.86	2.72	7.2	6.98	7.06	6.57	6.82	73.47	55.90	46.73	46.36

5. 2D Seismic Synthetics

The impact of high-velocity aluminum silicates on reflectivity was further assessed by modeling the seismic response of a simple VMS deposit consisting of a bimodal volcanic host rock background of basalt and rhyolite, a massive sulfide ore lens, and a subconcordant hydrothermal conduit (Figure 9). Two scenarios were tested: (1) A model in which the grade of the metamorphic overprint corresponds to peak metamorphic conditions inferred for the Lalor VMS deposit (600 °C, 6 kbar, [20]); and (2) a low-grade greenschist facies (350 °C, 2.5 kbar), equivalent of the first model, representative of the majority of VMS deposits discovered in the Canadian Shield. The seismic properties of the first model were computed from the mineral fractions of seven samples from the zone of intense hydrothermal alteration using the mixing laws described above. The normative minerals computed from the major oxide analyses of the same samples using CONSONORM_LG (CONSOREM (Consortium de recherche en exploration minérale—Mineral Exploration Research Consortium, de l'Université, Chicoutimi, QC, Canada) [35] (Table 6) were used to compute the seismic properties of the conduit consisting of the lower greenschist facies mineral assemblage of the second scenario. Normative mineral computations essentially provide an estimate of the idealized mineral composition of a rock, based on assumptions about the order of mineral formation (as defined, for example, by the order of crystallization of mineral phases from a melt) and known equilibrium phase relationships [36]. Normative mineral computations developed for metamorphic rocks (such as the CONSONORM_LG algorithm applied in this study) also honor metamorphic petrologic constraints, which limit mineral phases to those that can coexist in solid state under given pressure-temperature conditions [35]. The estimated normative mineral composition may differ from the visually observed mineral composition of the rock sample, dependent on the extent to which the assumptions that define the rules of the normative mineral computation are violated. The normative mineral computation starts by converting the weight fractions of the major oxides to mole fractions by dividing each oxide by its molecular weight. The computation then proceeds in a number of steps of prescribed order, in which the mole fractions are distributed among a preselected set of normative minerals until they eventually exhaust to zero. This involves a total of 12 computational steps for the CONSONORM_LG algorithm, subsequently allotting the mole fractions to sulfides, carbonates, Fe-Ti oxides, Al-Ca-Fe-K-Mg-Na silicates, quartz, and volatiles [35]. In the final step, the mole fractions of the normative minerals are multiplied by the appropriate formula weights and divided by the mineral densities to compute their volume fractions [36]. The normative minerals thus obtained for the hydrothermal conduit of the greenschist facies synthetic model were generalized into fewer classes and then renormalized to unity (Table 7). This involved the omission of all the fractions below 1%, the summation of Mg- and Fe-chlorite, as well as the summation of paragonite and sericite. Because neither the P-wave velocity measurements of pyrophyllite, nor the appropriate measurements of the elastic moduli required for computing it could be found in the literature, pyrophyllite was omitted from the analysis.

The properties of the least-altered host rocks (basalt and rhyolite) and ore for the greenschist facies modeling scenario were determined from wireline logs for the first scenario and were adjusted to reflect the appropriate pressure-temperature conditions for the second scenario using the average V_p and ρ of the least-altered basalt and rhyolite from the wireline logs acquired in the Flin Flon VMS camp [37]. The seismic properties of all modeled units, for both scenarios, are summarized in Table 8.

A total of 40 shot points equally distributed 20 m below the surface were modeled with an acoustic (P-wave velocity and density) finite-difference method based on a second-order approximation of the time derivatives, and a fourth-order approximation of the spatial derivatives was solved on a staggered grid. The seismic wavefield was sampled at 341 receivers also placed near the surface of the model every 10 m. The seismic source is a Ricker wavelet, with a center frequency of 70 Hz, which corresponds to the center frequency of the Lalor migrated volume [4]. Synthetic shot gathers were then migrated in depth using a reverse-time algorithm. Both modeling and reverse-time migration were conducted with Devito [38].

The strongest reflections are in both the greenschist and amphibolite facies scenarios, associated with the ore zone (Figure 9, Table 9). For the amphibolite scenario, the reflection beneath the ore zone includes constructive interference from the conduit-basalt contact. Note the enhanced reflectivity of the basalt-rhyolite contacts in the amphibolite facies scenario, due to the significant increase of P-wave velocity in basalt (a 40% increase in reflectivity in comparison with the greenschist scenario, Table 9). The most significant difference in acoustic impedance contrast between the two scenarios is observed at the contacts between the conduit and felsic host rocks. For the amphibolite facies scenario, the reflectivity of the conduit-rhyolite contacts increases by 75% (Table 9) with respect to the reflectivity of these contacts in the greenschist facies scenario, becoming as large as the impedance contrast across the basalt-rhyolite contacts (Table 8). In contrast, in the greenschist facies scenario, the conduit is weakly reflective when juxtaposed against rhyolite (Table 8). Seismic reflections at conduit-basalt contacts are probably not detectable in both scenarios, considering the 6% rule-of-thumb threshold for a strong amplitude-normal seismic reflection [2].

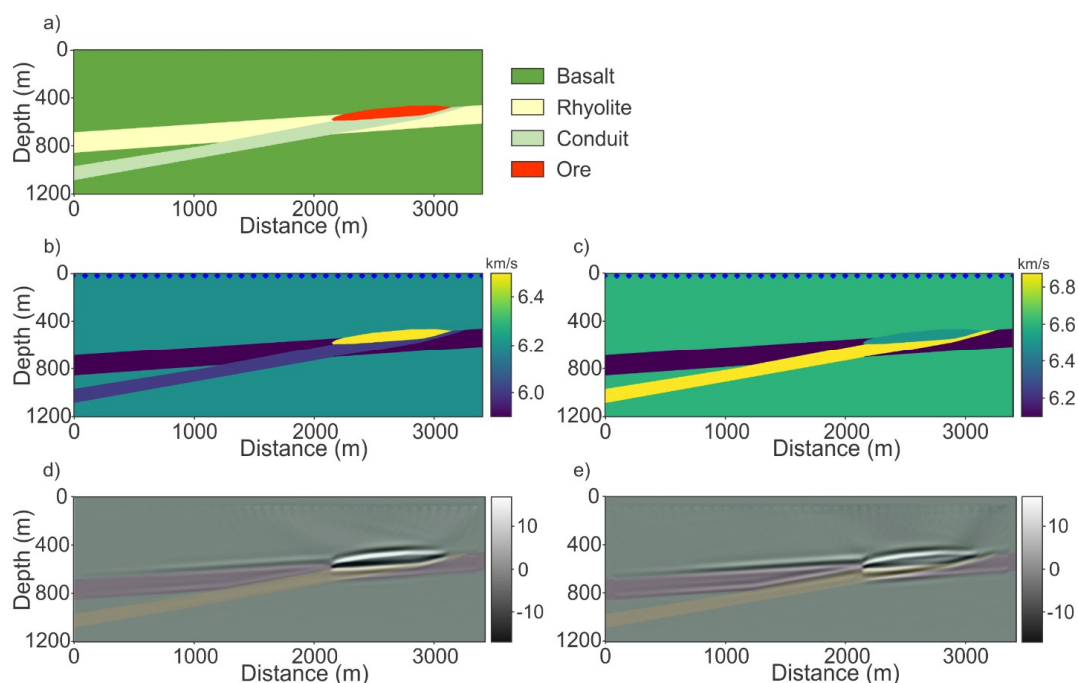


Figure 9. Models used for seismic synthetics. (a) Model of a VMS deposit with a subconcordant hydrothermal conduit; (b) P-wave velocity model for greenschist facies conditions; (c) P-wave velocity model for amphibolite facies conditions; (d) processed seismic forward modeling profile for greenschist facies conditions; (e) processed seismic forward modeling profile for amphibolite conditions. See text for details on the modeling procedure.

Table 6. Major oxide analyses from the footwall hydrothermal alteration zone.

Sample	SiO ₂	Al ₂ O ₃	Fe ₂ O ₃	FeO	CaO	K ₂ O	Na ₂ O	MgO	MnO	TiO ₂	P ₂ O ₅	CO ₂	S	LOI	Total
GSC-Lalor-MD023	49.91	18.45	0.36	10.4	4.41	2.8	0.53	8.54	0.317	0.563	0.21	1.45	0.22	3.07	100.7
GSC-Lalor-MD041	61.73	13.82	2.26	10.1	0.69	1.44	0.18	7.31	0.375	0.495	0.14	0.2	1.17	1.3	101
GSC-Lalor-MD099	61.95	13.31	0.94	11.2	2.89	0.44	0.29	5.58	0.182	0.599	0.21	0.11	1.34	0.83	99.68
GSC-Lalor-MD110	42.14	21.29	0.05	12.6	0.57	0.8	0.15	14.88	0.241	0.532	0.22	0.06	1.33	3.71	98.59
GSC-Lalor-MD160	67.3	12.48	0.17	7	0.44	1.21	0.08	8.78	0.166	0.618	0.24	0.03	0.005	0.94	100.2
GSC-Lalor-MD165	65.85	14.19	1.54	7	0.49	1.49	0.32	6.43	0.31	0.599	0.18	0.07	0.02	0.84	100
GSC-Lalor-MD218	57.85	12.58	0.57	13.7	1.27	0.03	0.07	10.23	0.264	1.081	0.77	0.05	0.08	0.37	100.3

Table 7. Greenschist facies normative minerals for modeling the hydrothermal conduit.

Sample	Alb	Chl	Ep	Qtz	Ser
GSC-Lalor-MD023	0.17	0.44	0.15	0.18	0.05
GSC-Lalor-MD041	0.00	0.40	0.01	0.44	0.15
GSC-Lalor-MD099	0.00	0.37	0.09	0.46	0.08
GSC-Lalor-MD110	0.00	0.80	0.00	0.08	0.11
GSC-Lalor-MD160	0.00	0.39	0.00	0.50	0.11
GSC-Lalor-MD165	0.00	0.34	0.00	0.48	0.18
GSC-Lalor-MD218	0.00	0.58	0.00	0.40	0.01
Mean	0.02	0.47	0.04	0.37	0.10

Table 8. Seismic rock properties used for synthetic modeling.

Amphibolite Facies						Greenschist Facies				
Unit	Mineral	%	ρ (g/cm ³)	V_p (km/s)	Ω (kg·m ⁻² ·s ⁻¹ × 10 ⁻⁶)	Mineral	%	ρ (g/cm ³)	V_p (km/s)	Ω (kg·m ⁻² ·s ⁻¹ × 10 ⁻⁶)
Conduit	Crd	28	2.65	8.71	23.1					
	Grt	3	4.20	8.55	35.9	Ep	4	3.40	7.43	25.3
	Am	27	2.95	6.95	20.5	Chl	47	3.05	6.01	18.3
	Bt	9	3.15	5.26	16.6	Ser	10	2.81	6.30	17.7
	An	3	2.73	7.25	19.8	Alb	2	2.63	6.30	16.6
	Qtz	30	2.65	6.05	16.0	Qtz	37	2.65	6.05	16.0
	Py	1	5.04	8.12	40.9	Py	1	5.04	8.12	40.9
	Mixture modelled		2.88	6.87	19.8	Mixture modelled		2.90	6.01	17.4
Basalt			3.00	6.60	19.8			2.90	6.20	18.0
Rhyolite			2.80	6.10	17.1			2.75	5.90	16.2
Ore			4.20	6.50	27.3			4.20	6.50	27.3

Table 9. Seismic reflection coefficients R ($R = (\Omega_2 - \Omega_1)/(\Omega_1 + \Omega_2) \times 100\%$, where Ω_1 and Ω_2 are the acoustic impedances of the rock materials in contact with each other) between the ore, conduit, and host rocks and their differences for the acoustic finite difference models for the greenschist and amphibolite facies scenarios.

Model Contact (Figure 9a)	R Greenschist Facies (%)	R Amphibolite Facies (%)	Difference (%)
sulfide ore/basalt	21	16	-31
sulfide ore/rhyolite	26	23	-13
basalt/rhyolite	5	7	+40
conduit/basalt	2	0	-
conduit/rhyolite	4	7	+75

6. Seismic Interpretation

In 2013, the Geological Survey of Canada acquired a 3D seismic survey to characterize the three-dimensional structure of the Lalor deposit and its host rock envelope. The 3D survey covers an area of approximately 16 km² (Figure 1) and includes 908 shot points and 2685 receiver stations. The many shot points located northeast of the deposit provided sufficient ore zone illumination from the down-dip direction to produce a high-quality image of the deposit and alteration zone. Details on the acquisition, data processing, and initial interpretation of the 3D seismic data are found in [4]. The seismic survey allowed the detection of the massive zinc-rich zones and identified strong reflectivity in the altered footwall rocks at contacts between metamorphosed rocks with felsic and mafic protoliths [4]. Figure 10 shows inline 1098 from the 3D seismic volume and a coincident section from a 3D geological model, representing lithofacies derived from the Zr/Ti immobile element ratio. Arrows A and B point to reflections occurring at contacts between felsic and mafic rocks/protoliths in the least and most altered footwall rocks. Reflection B has higher amplitudes and is more continuous than reflection A. Arrow C indicates a series of strong reflections downdip of the alteration zone in

the geological model and represents a possible continuation of strong footwall alteration at depths. At even greater depth, the strong reflections indicated with label D could be related to a structural repeat of the same hydrothermal alteration conduit or a conduit-sulfide mount hosted in an underlying lithostratigraphic interval. The abrupt termination updip of reflections D, almost directly beneath the deposit, supports both interpretations. Alternatively, reflections D may result from lithological variations. Following our interpretation, the areas indicated with arrow C and possibly arrow D, are rocks characterized by intense hydrothermal alteration, with high economical potential. At Lalor, examples of such potential are the disseminated gold-rich zones that, contrary to the massive sulfide zones of this deposit, are not directly detected with seismic or other geophysical methods, because these relatively narrow zones with low percentages of sulfides do not experience a sufficient change in seismic rock properties to generate reflections. The disseminated zones are nevertheless found in metamorphosed and altered footwall rocks, characterized with an enhanced seismic reflectivity, originating from hydrothermally-altered rocks with a significant abundance of aluminum silicates with high V_p (cordierite and garnet).

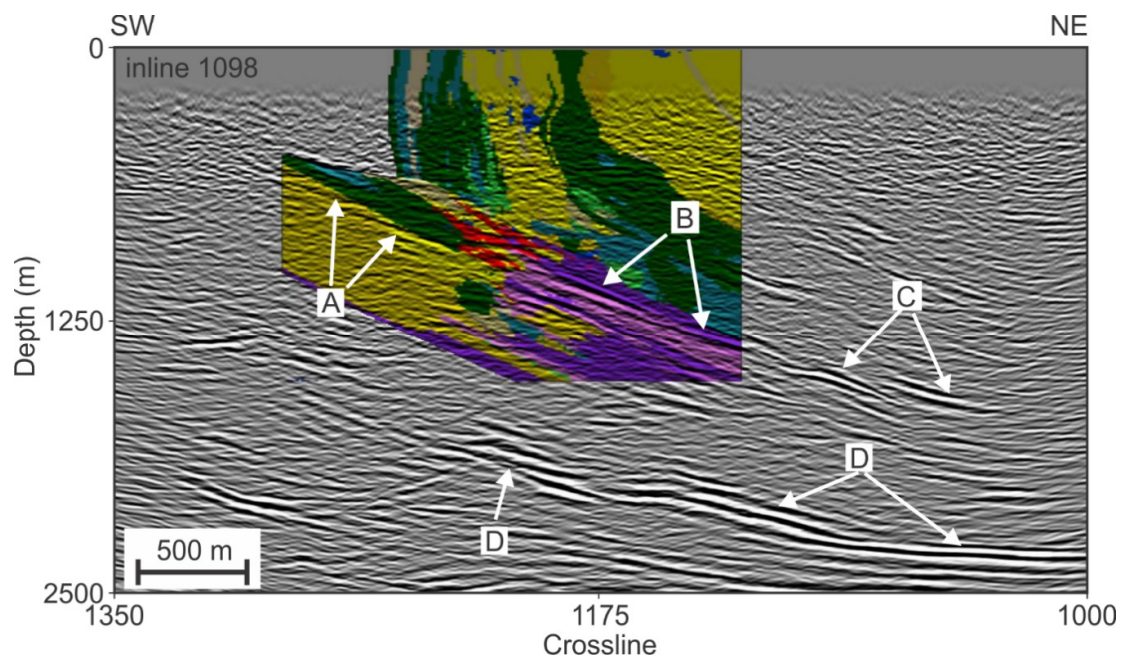


Figure 10. Inline 1089 from the final migrated seismic volume with a coincident section from the 3D geological model overlaid on top of the seismic section. See text for details on events indicated by arrows. Modified from [4].

7. Discussion

Four distinct processes control the variation in seismic rock properties throughout the geological history of the Lalor VMS deposit, including (1) the protolith composition resulting from the extrusion and deposition of volcanic and volcanoclastic rocks of different composition on the paleo seafloor, (2) sulfide mineralization, (3) host rock alteration during the subsequent flow of hydrothermal fluids through the ocean floor, and (4) metamorphic recrystallization after the emplacement and subsequent tectonic burial of the VMS deposit within an orogenic belt. All four processes (in addition to weathering and unloading when the deposit is exhumed to the surface) will affect seismic rock properties, although the first two appear to be dominant, which explains why they are dominantly reported in the hard rock seismic exploration literature [1–3]. The additional effects on seismic rock properties of the latter two processes are much more challenging to assess. Firstly, many more silicate species, many of which are also found in their unaltered equivalents, occur in association with VMS deposits, in comparison to the few sulfide species that define the ore zones. Secondly, many of the silicates

involved have much stronger anisotropies in velocity and will likely react to other species as a result of subsequent metamorphic recrystallization. Nonetheless, the SEM-EDS analysis, although applied on a limited number of samples ($n = 11$), was effective for interpreting the relationships between the mineral abundance and measured seismic rock properties of hydrothermally-altered rocks, allowing the corroboration of the empirical relationships inferred from the much larger wireline seismic property datasets.

SEM-EDS analysis outperforms traditional point counting under the microscope for a number of reasons: (1) Contrary to point counts, the entire thin section is scanned, leading to more robust abundance estimates; (2) the visual discrimination of certain minerals can be difficult or unpractical based on optical microscopic diagnostic criteria, such as the discrimination between cordierite and quartz, and between different feldspars and amphiboles; (3) SEM-EDS, in addition to mineral identification, also provides the chemical composition of the classified minerals, which potentially allows for a more precise assessment of the mineral seismic properties for mineral compositional series, such as feldspars and amphiboles. Given the long scanning times, exceeding on average 6 hours and an additional 1.5 h for classification per sample, the method is, however, time-consuming and therefore costly.

Alternative approaches based on analyzing the relationships between seismic rock property measurements and geochemical proxies for alteration, as previously attempted in [39], are limited in scope, because, as shown in the forward modeling study, similar ranges in these proxies could (depending on the metamorphic grade) show large variations in mineral seismic properties. Therefore, estimates of mineral abundance are essential to progress the understanding of the seismic response of hydrothermal alteration. A solution that would bypass laborious mineralogical analysis is to obtain theoretical mineral abundance estimates through normative mineral computation, but these methods are fraught with modeling limitations themselves, as they either lead to non-unique solutions or, when additional constraints (such as pressure and temperature) are involved, yield mineral species that significantly deviate from those observed in practice. Future studies may explore upscaling approaches where the results of the SEM-EDS analyses are used to define the endmembers in user-defined normative mineral computations, such as proposed in [40].

Several factors contribute to the uncertainty of the seismic property mixture models, including (1) the variability in the mineralogical composition between the mini-core and thin section slabs cut at different locations from a 20–30 cm piece of drill core; (2) errors in the SEM-EDS analyses, including violations of the isotropic assumption of random sampling design that justify the use of areal percentages in estimating volumetric percentages of foliated rocks; (3) errors in the seismic rock property measurements; (4) violation of the assumptions of homogeneous and isotropic mixtures used to compute the Voigt and Reuss bounds related to anisotropy in mineral seismic velocities; and (5) uncertainty in the mineral seismic properties, with respect to the specific chemical composition of the mineral analyzed in the sample. The good fit obtained for density suggests that the effects of factors 1 and 2 (and 3 for density) are relatively small, although the two outliers (Figure 6) could be explained by these factors. Errors in the V_p measurements are also not a dominant factor, as these measurements are generally considered accurate to 0.5–1% [5]. The fact that a significant number of P-wave velocity measurements (4 out of 8, excluding outliers in density modeling, see inset Figure 7) fall outside the theoretical Voigt and Reuss bounds suggests that factors 4 and 5 likely play a dominant role and violate the assumptions of homogeneous and isotropic mineral components. Indeed, many of the samples show preferred orientation of mineral constituents, such as amphibole and biotite, as they are aligned along the gneissosity, pointing to large anisotropies in the rock fabric (Figure 5). These anisotropic effects on seismic rock properties have not been assessed in our study. They can be estimated by measuring seismic velocities in three mutually orthogonal directions (see [41] for an example of the Anabel shear zone of the Flin Flon greenstone belt, about 100 km to the west of the Lalor VMS deposit). Variations in the concentrations of Fe and Mg in minerals such as cordierite, chlorite, garnet, and particularly amphibole, significantly impact their corresponding seismic properties. Hence,

mineral seismic property measurements over a range of chemical compositions, which are currently not available in the literature, may help in reducing the uncertainty in seismic property models dominated by variations in silicate minerals.

8. Conclusions

The effects of hydrothermal alteration on the density, P-wave velocity, and seismic response of the Lalor VMS deposit have been investigated using lithofacies log descriptions, γ - γ density, P-wave velocity logs, geochemical data, and estimates of mineral abundances from SEM-EDS analyses of drill core samples. Our findings are summarized as follows:

1. Variations in host rock composition and massive sulfide ore are the main controlling factors of acoustic impedance contrasts, resulting in high-amplitude reflections in the Lalor 3D seismic data, regardless if rocks are hydrothermally-altered or not.
2. Metamorphism at amphibolite facies of hydrothermally altered intermediate and mafic protoliths induces a superposed secondary effect on seismic rock properties, in which P-wave velocity increases with the intensity of alteration, whereas density remains nearly constant or slightly decreases.
3. In combination, density and P-wave velocity mark a steep, low-density trend towards $V_p = 8.71$ km/s and $\rho = 2.65$ g/cm³, corresponding to cordierite, which has a unique low density, high P-wave velocity signature in comparison to other silicate minerals. Cordierite, as well as other aluminum silicates, such as garnet, kyanite, sillimanite, and staurolite in volcanic protoliths, are diagnostic for hydrothermally-altered rocks that have been metamorphosed in the middle to higher amphibolite facies.
4. The low-density, high-velocity trend observed in the wireline log data is corroborated by the SEM-EDS analysis of the thin sections, which show that cordierite, with its anomalous high bulk modulus over density ratio, is by far the most abundant high-velocity mineral.
5. Seismic synthetics obtained by acoustic finite-difference modeling experiments for a VMS model with a amphibolite facies metamorphic overprint, show enhanced seismic reflectivity at conduit-felsic host rock contacts in comparison to seismic synthetics obtained from the same model with a greenschist facies metamorphic overprint.
6. The enhanced seismic signature caused by hydrothermal alteration can be recognized in the Lalor seismic data, demonstrating the potential of seismic surveys in its detection.

Author Contributions: E.S. analyzed the relationships between the lithofacies, drill core litho-geochemistry, and seismic properties from wireline logs and computed the seismic rock property mixture models, including the ones subjected to seismic forward modeling. P.H. conducted the SEM-EDS analyses of the thin sections, which included estimating the mineral abundance. G.B. conducted the forward seismic modeling experiments. E.S. and G.B. reinterpreted the 3D seismic data.

Funding: This research received no external funding.

Acknowledgments: We gratefully acknowledge the support of Hudbay Minerals Inc. in providing access to the drill hole data of the Lalor mine camp and for sharing their expertise on the Lalor VMS deposit. We are grateful to Antoine Caté and Patrick Mercier-Langevin for sharing their expertise on the geology of the Lalor VMS deposit and their assistance in preparing drill core sample materials for whole rock geochemical and SEM-EDS analysis. We thank Randy Enkin and Matt Salisbury for conducting the drill core physical rock property measurements. This paper benefitted from discussions with Don White and Rob Berman, as well as, the critical comments of two anonymous reviewers. We acknowledge funding of this research by Natural Resources Canada's Targeted Geoscience Initiative programs (phase 4 and phase 5). This is Geological Survey of Canada contribution no. 20190108.

Conflicts of Interest: The authors declare no conflict of interest. Hudbay Minerals provided the drill hole data used in this study and 3D models of the sulfide ore lenses.

Appendix A

The co-registration of geochemical analyses and the lithofacies classifications of drill core samples with P-wave velocity and γ - γ density log samples was accomplished by matching their corresponding Microsoft Access® database records on drill hole collar identifier and sample depth using a threshold distance criterion of 30 cm. In standard query language (SQL), this query was defined as follows:

```
SELECT WirelineLogs.HOLEID, WirelineLogs.Depth, GeochemLithofacies.*, WirelineLogs.
Density, WirelineLogs.P_Wave_Velocity
```

```
FROM GeochemLithofacies INNER JOIN WirelineLogs ON GeochemLithofacies.HoleID =
WirelineLogs.HOLEID
```

```
WHERE(((Sqr((WirelineLogs.[Depth]-GeochemLithofacies.[Depth])^2))<0.3));
```

With the following schemas for the tables WirelineLogs and GeochemLithofacies:

Table A1. Matched database fields of WirelineLogs and GeochemLithofacies tables.

WirelineLogs	GeochemLithofacies
HOLEID	HOLEID
Depth	Depth
Density	Zr/Ti
P-Wave_Velocity	AI (Ishikawa index)
	CCPI (Chlorite-carbonate-pyrite index)
	Lithofacies class

where * refers to a wildcard character used for the selection of all database fields.

References

- Salisbury, M.H.; Harvey, C.W.; Matthews, L. The Acoustic Properties of Ores and Host Rocks in Hardrock Terranes. In *Hard Rock Seismic Exploration*; Eaton, D.W., Milkereit, B., Salisbury, M.H., Eds.; Society of Exploration Geophysics Books: Tulsa, OK, USA, 2003; pp. 9–19.
- Snyder, D.; Salisbury, M.H. Application of Seismic Methods to Mineral Exploration. In *Mineral Deposits of Canada: A Synthesis of Major Deposit-Types, District Metallogeny, the Evolution of Geological Provinces, and Exploration Methods*; Special Publication No. 5; Goodfellow, W.D., Ed.; Geological Association of Canada, Mineral Deposits Division: Ottawa, ON, Canada, 2007; pp. 971–982.
- Malehmir, A.; Durrheim, R.; Bellefleur, G.; Urosevic, M.; Juhlin, C.; White, D.J.; Milkereit, B.; Campbell, G. Seismic methods in mineral exploration and mine planning: A general overview of past and present case histories and a look into the future. *Geophysics* **2012**, *77*, WC173–WC190. [[CrossRef](#)]
- Bellefleur, G.; Schetselaar, E.; White, D.; Miah, K.; Dueck, P. 3D Seismic imaging of the Lalor volcanogenic massive sulphide deposit, Manitoba, Canada. *Geophys. Prospect.* **2015**, *63*, 813–832. [[CrossRef](#)]
- Schetselaar, E.; Bellefleur, G.; Craven, J.; Roots, E.; Cheraghi, S.; Shamsipour, P.; Caté, A.; Mercier-Langevin, P.; El Goumi, N.; Enkin, R.; et al. Geologically Driven 3D Modelling of Physical Rock Properties in Support of Interpreting the Seismic Response of the Lalor Volcanogenic Massive Sulphide Deposit, Snow Lake, Manitoba, Canada. In *Characterization of Ore-Forming Systems from Geological, Geochemical and Geophysical Studies*; Special Publications 453(1):SP453.5; Gessner, K., Blenkinsop, T.G., Sorjonen-Ward, P., Eds.; Geological Society of London: Bath, UK, 2017; pp. 57–82. [[CrossRef](#)]
- Bailes, A.H.; Galley, A.G. Evolution of the Paleoproterozoic Snow Lake arc assemblage and geodynamic setting for associated volcanic-hosted massive sulphide deposits, Flin Flon Belt, Manitoba, Canada. *Can. J. Earth Sci.* **2000**, *36*, 1789–1805. [[CrossRef](#)]
- Kraus, J.; Williams, P.F. Structural development of the Snow Lake allochthon and its role in the evolution of the southeastern Trans-Hudson Orogen in Manitoba, central Canada. *Can. J. Earth Sci.* **1999**, *36*, 1881–1899. [[CrossRef](#)]
- Stewart, M.S.; Lafrance, B.; Gibson, H.L. Early thrusting and folding in the Snow Lake camp, Manitoba: Tectonic implications and effects on volcanogenic massive sulfide deposits. *Can. J. Earth Sci.* **2018**, *55*, 935–957. [[CrossRef](#)]

9. Bailes, A.H.; Galley, A.G. *Geology of the Chisel-Anderson Lakes Area, Snow Lake, Manitoba (NTS Areas 63K16SW and West Half of 63J13SE)*; Geoscientific Map 2007-1, Colour Map with Accompanying Notes, scale 1: 20 000; Manitoba Science, Technology, Energy and Mines Manitoba Geological Survey: Winnipeg, MB, Canada, 2007.
10. Bailes, A.; Rubingh, K.; Gagné, S.; Taylor, G.; Galley, A.; Bernauer, S.; Simms, D. Volcanological and Structural Setting of Paleoproterozoic VMS and Gold Deposit at Snow Lake, Manitoba. In Proceedings of the Geological Association of Canada-Mineralogical Association of Canada Joint Annual Meeting, St. John's, CA, Canada, 27–29 May 2012; Field Trip Guidebook FT-A2; Open File OF2013-3. Manitoba Innovation, Energy and Mines, Manitoba Geological Survey: Winnipeg, MB, Canada, 2013. 63p.
11. Bailes, A.H.; Galley, A.G.; Paradis, S.; Taylor, B.E. Variations in large synvolcanic alteration zones at Snow Lake, Manitoba, Canada, with proximity to associated volcanogenic massive sulfide deposits. *Econ. Geol.* **2016**, *111*, 933–962. [[CrossRef](#)]
12. Caté, A.; Mercier-Langevin, P.; Ross, P.S.; Duff, S.; Hannington, M.; Dubé, B.; Gagné, S. *The Paleoproterozoic Lalor VMS Deposit, Snow Lake, Manitoba: Observations on the Nature and Architecture of the Gold and Base Metal-Rich Ore Zones and Associated Alteration*; Open File Report 7483; Geological Survey of Canada: Ottawa, ON, Canada, 2013; 19p. [[CrossRef](#)]
13. Duff, S.; Hannington, M.D.; Caté, A.; Mercier-Langevin, P.; Kjarsgaard, I.M. Major Ore Types of the Paleoproterozoic Lalor Auriferous Volcanogenic Massive Sulphide Deposit, Snow Lake, Manitoba. In *Targeted Geoscience Initiative 4: Contributions to the Understanding of Volcanogenic Massive Sulphide Deposit genesis and Exploration Methods Development*; Open File 7853; Peter, J.M., Mercier-Langevin, P., Eds.; Geological Survey of Canada: Ottawa, ON, Canada, 2015; pp. 147–170. [[CrossRef](#)]
14. Caté, A.; Mercier-Langevin, P.; Ross, P.-S.; Duff, S.; Hannington, M.D.; Dubé, B.; Gagné, S. Geology and Au Enrichment Processes at the Paleoproterozoic Lalor Auriferous Volcanogenic Massive Sulphide Deposit, Snow Lake, Manitoba. In *Targeted Geoscience Initiative 4: Contributions to the Understanding of Volcanogenic Massive Sulphide Deposit Genesis and Exploration Methods Development*; Open File 7853; Peter, J.M., Mercier-Langevin, P., Eds.; Geological Survey of Canada: Ottawa, ON, Canada, 2015; pp. 131–145. [[CrossRef](#)]
15. Caté, A.; Mercier-Langevin, P.; Ross, P.S.; Simms, D. *Structural Controls on Geometry and Ore Distribution in the Lalor Auriferous VMS Deposit. Snow Lake, West-Central Manitoba (part of NTS 63K16): Preliminary Results from Underground Mapping*; Report of Activities; Manitoba Science, Technology, Energy and Mines, Manitoba, Geological Survey: Winnipeg, MB, Canada, 2014; pp. 104–115.
16. Ramsay, J.G. *Folding and Fracturing of Rocks*; McGraw-Hill: New York, NY, USA, 1967; 568p.
17. McClay, K. *The Mapping of Geological Structures*; John Wiley & Sons Ltd.: Sussex, UK, 1991; 161p.
18. Schetselaar, E.; Shamsipour, P. Acquisition, Processing, and Interpretation of Gravity Drill Hole Data. In *Targeted Geoscience Initiative 4: A Synthesis of the Methodology Project at the Lalor VMS Deposit, Manitoba*; Open File 7863; Bellefleur, G., Schetselaar, E., Craven, J.A., Eds.; Geological Survey of Canada: Ottawa, ON, Canada, 2014; pp. 32–37. [[CrossRef](#)]
19. Cas, R.A.F.; Wright, J.V. *Volcanic Successions Modern and Ancient: A Geological Approach to Processes, Products and Successions*; Chapman & Hall: London, UK, 1987; 527p.
20. Caté, A. *Geology of the Paleoproterozoic Zn-Cu-Au Lalor Volcanogenic Massive Sulphide Deposit and Its Gold-Rich Lenses, Snow Lake, Manitoba*. Ph.D. Thesis, Institut National de la Recherche Scientifique, Université du Québec, Québec City, QC, Canada, 2017; 430p.
21. Large, R.R.; Gemmill, J.B.; Paulick, H. The alteration box plot: A simple approach to understand the relationship between alteration mineralogy and lithogeochemistry associated with volcanic-hosted massive sulfide deposits. *Econ. Geol.* **2001**, *96*, 957–971. [[CrossRef](#)]
22. Bristol, C.C.; Froese, E. Highly metamorphosed altered rocks associated with the Osborne Lake volcanogenic massive sulfide deposit, Snow Lake area, Manitoba. *Can. Mineral.* **1989**, *27*, 593–600.
23. Menard, T.; Gordon, T.M. Metamorphic P-T paths from the Eastern Flin Flon belt and Kiseynew domain Snow Lake, Manitoba. *Can. Mineral.* **1997**, *35*, 1093–1115.
24. Pirrie, D.; Rollinson, G.K. Unlocking the applications of automated mineral analysis. *Geol. Today* **2011**, *27*, 226–235. [[CrossRef](#)]
25. Newbury, D.E.; Nicholas, W.M.R. Is Scanning Electron Microscopy/Energy Dispersive X-ray Spectrometry (SEM/EDS) Quantitative? *Scanning* **2013**, *35*, 141–168. [[CrossRef](#)] [[PubMed](#)]
26. Delesse, M.A. Procédé mécanique pour déterminer la composition des roches. *Comptes Rendus Acad. Sci. (Paris)* **1847**, *25*, 544–545.

27. Oxford Instruments Applications Library: Automated Analysis of Sections of Geological Materials. Available online: <https://nano.oxinst.com/campaigns/downloads/automated-analysis-of-sections-of-geological-materialsOxford> (accessed on 20 February 2019).
28. Mavko, G.; Mukerji, T.; Dvorkin, J. *The Rock Physics Handbook*, 2nd ed.; Tools for Seismic Analysis of Porous Media; Cambridge University Press: Cambridge, UK, 2014; 511p.
29. Schmitt, D.R. Geophysical Properties of the Near Surface Earth: Seismic Properties. In *Treatise on Geophysics*, 2nd ed.; Schubert, G., Ed.; Elsevier: Oxford, UK, 2015; Volume 11, pp. 43–87.
30. Ji, S.; Wang, Q.; Xia, B. *Handbook of Seismic Properties of Minerals, Rocks and Ores*; École Polytechnique de Montreal: Montreal, QC, Canada, 2002; 630p.
31. Mineral Website, Mineral Properties. Available online: <http://webmineral.com/determin.shtml> (accessed on 23 February 2019).
32. Kern, H.; Mengel, K.; Strauss, K.W.; Ivankina, T.I.; Nikitin, A.N.; Kukkonen, I.T. Elastic wave velocities, chemistry and modal mineralogy of crustal rocks sampled by the Outokumpu Scientific Drill Hole: Evidence from lab measurements and modeling. *Phys. Earth Planet. Inter.* **2009**, *175*, 151–166. [[CrossRef](#)]
33. Toohill, K.; Siegesmund, S.; Bass, J.D. Sound velocities and elasticity of cordierite and implications for deep crustal seismic anisotropy. *J. Phys. Chem. Minim.* **1999**, *26*, 333–343. [[CrossRef](#)]
34. Salisbury, M.H.; Milkereit, B.; Ascough, G.; Adair, R.; Matthews, L.; Schmitt, D.R.; Mwenifumbo, J.; Eaton, D.W.; Wu, J. Physical properties and seismic imaging of massive sulfides. *Geophysics* **2006**, *65*, 18–82. [[CrossRef](#)]
35. Trepannier, S.; Mathieu, L.; Daigneault, R. CONSONORM_LG: New Normative Minerals and Alteration indices for low-grade metamorphic rocks. *Econ. Geol.* **2015**, *10*, 2127–2138. [[CrossRef](#)]
36. Philpotts, A.R. *Principles of Igneous and Metamorphic Petrology*; Prentice Hall: Upper Saddle River, NJ, USA, 1990; 498p.
37. White, D.J.; Mwenifumbo, C.J.; Salisbury, M.H. Seismic Properties of Rocks from the Flin Flon Volcanogenic Massive Sulfide Camp. *Econ. Geol.* **2016**, *111*, 913–931. [[CrossRef](#)]
38. Louboutin, M.; Lange, M.; Luporini, F.; Kukreja, N.; Witte, P.A.; Herrmann, F.J.; Veleško, P.; Gorman, G.J. Devito: An embedded domain-specific language for finite differences and geophysical exploration. *Geosci. Model Dev.* **2018**, *12*, 1165–1187. Available online: <https://arxiv.org/abs/1808.01995v1> (accessed on 11 January 2019). [[CrossRef](#)]
39. Schetselaar, E.M.; Bellefleur, G.; Craven, J.A.; Ansari, S.M.; Enkin, R.J. Elucidating Mineralizing Fluid Pathways from the Geophysical Responses to Hydrothermal Alteration: Integrated 3D Modelling of Litho-geochemical, Petrophysical, Seismic and Magnetotelluric Data, Lalor Volcanogenic Massive Sulphide Deposit, Manitoba. In *Targeted Geoscience Initiative: 2017 Report of Activities*; Open File 8358; Rogers, N., Ed.; Geological Survey of Canada: Ottawa, ON, Canada, 2018; Volume 1, pp. 229–242. [[CrossRef](#)]
40. Currie, K.L. GENORM: A generalized norm calculation. *Comput. Geosci.* **1991**, *1*, 77–89. [[CrossRef](#)]
41. Cholach, P.Y.; Molyneux, J.B.; Schmitt, D.R. Flin Flon Belt seismic anisotropy: Elastic symmetry, heterogeneity, and shear-wave splitting. *Can. J. Earth Sci.* **2005**, *42*, 533–554. [[CrossRef](#)]

